Observation and modeling of the winter coastal oceanic circulation in the Gulf of Lion under wind conditions influenced by the continental orography (FETCH experiment)

C. Estournel

Observation and modeling of the winter coastal oceanic circulation in the Gulf of Lion under wind conditions influenced by the continental orography (FETCH experiment)

C. Estournel
Laboratoire d'Aérologie, Centre National de la Recherche Scientifique-Université Paul Sabatier, Toulouse, France

X. Durrieu de Madron
CEFREM, Centre National de la Recherche Scientifique-Université de Perpignan, Perpignan, France

P. Marsaleix, F. Auclair, C. Julliand, and R. Vehil
Laboratoire d'Aérologie, Centre National de la Recherche Scientifique-Université Paul Sabatier, Toulouse, France

Received 25 January 2001; revised 24 September 2001; accepted 15 October 2001; published 21 February 2003.

[1] Hydrological and currentmeter observations were collected on the continental shelf and slope of the Gulf of Lion during the FETCH experiment (13 March to 15 April 1998). Results from the first part of the cruise, characterized by strong northern winds, are presented. The hydrological structures evidence well-mixed water masses on the eastern and western ends of the shelf. In the central part, the situation is more complex, with the influence of the Rhône river's freshwater plume in the first 40 m of the water column and, closer from the bottom, with the confrontation of downwelled coastal cold water and upwelled warmer and saltier slope water. Current measurements show the path of the cyclonic circulation along the slope, which is part of the general circulation of the western Mediterranean, and suggest the presence of large and temporary eddies on the shelf. This oceanic circulation is simulated with a free surface three-dimensional model using realistic forcing. The model outputs are in agreement with the main hydrological and circulation patterns. The results further indicate that coastal eddies are generated by the mesoscale structure of the wind field. *INDEX TERMS:* 4219 Oceanography: General: Continental shelf processes; 4504 Oceanography: Physical: Air/sea interactions (0312); *KEYWORDS:* Gulf of Lion, coastal circulation, wind curl, shelf-slope exchanges

Citation: Estournel, C., X. Durrieu de Madron, P. Marsaleix, F. Auclair, C. Julliand, and R. Vehil, Observation and modeling of the winter coastal oceanic circulation in the Gulf of Lion under wind conditions influenced by the continental orography, (FETCH experiment), *J. Geophys. Res.*, *108*(C3), 8059, doi:10.1029/2001JC000825, 2003.

1. Introduction

[2] Nowadays, the oceanic circulation in the coastal zone is the object of an increased attention because of (i) the evolving demographic pressure and the concomitant sewage of pollutants that imperil the equilibrium of the coastal ecosystems, and (ii) the expected role of these highly productive ecosystems on greenhouse gases cycle [*Hall and Smith*, 1996].

[3] Hence, the identification and the modeling of the major features of the coastal circulation appear as an important stake to assess their effect on the ecosystems functioning and to provide a forecasting tool for their rational management. It is clear that, similarly to the operational oceanography programs developed for the open sea, these objectives can be achieved only by coupling observations and model.

[4] Such an approach uses several steps. First, one needs to make sure that the models with their operating procedure (initialization, forcing) are able to reproduce the main characteristics of the circulation for the study area. Second, it is necessary to identify the critical points (e.g., boundary conditions, atmospheric forcing, and stratification) which will require supplementary field observations.

[5] Following the aforementioned methodological approach, the present work aims at assessing the ability of the SYMPHONIE model to reproduce the major features of the Gulf of Lion circulation observed during a cruise. It further attempts to analyze the role of the different forcing (heat flux, freshwater input, wind) on model results, and to propose a functioning scheme that can be applied beyond the present experiment.

[6] The Gulf of Lion is a fairly large continental margin (Figure 1) where intense forcings coexist:

1. strong continental winds, the Mistral and the Tramontane, whose direction is constrained by the orography. The Mistral is a northern wind channeled by the Rhône river valley in the northern part of the Gulf, whereas the Tramontane is a northwestern wind channeled by the Naurouze passage, blowing along the Roussillon coasts

0148-0227/03/2001JC000825

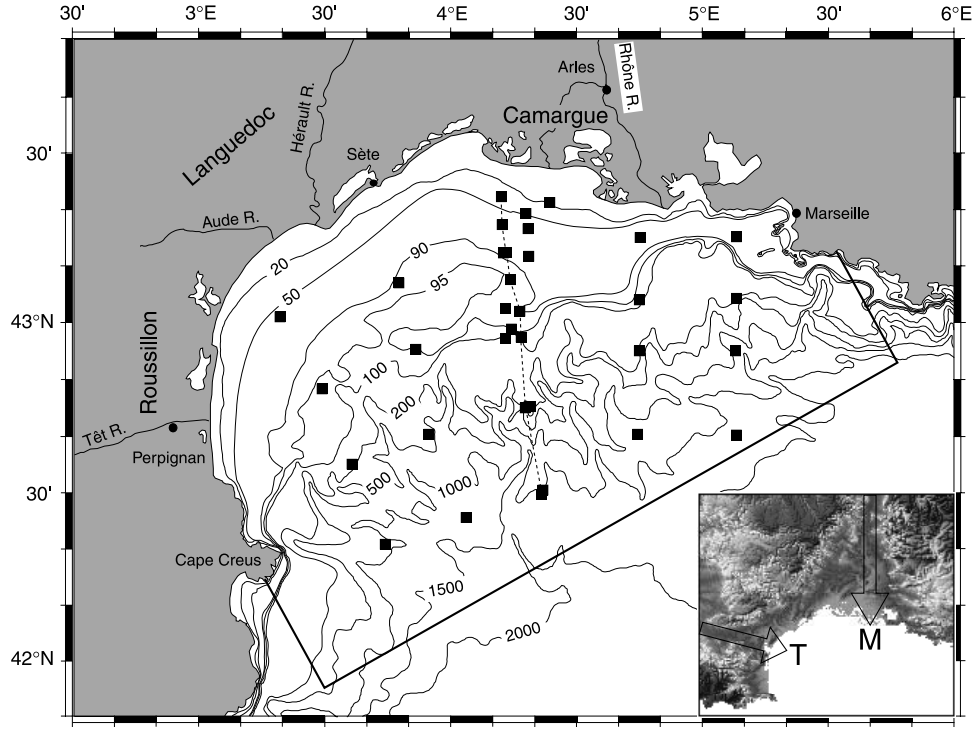

Figure 1. Map of the Gulf of Lion and hydrological station network performed during the FETCH cruise. The box delineates the limits of the model's domain. The insert indicates the origin of the two main continental winds: the Mistral (M) and the Tramontane (T).

(Figure 1). The effect of these cold and dry winds on the cooling of the surface waters and the dense water formation in winter is well-known [*Lacombe and Tchernia*, 1974; *Hua and Thomasset*, 1983; *Millot*, 1990; *Madec et al.*, 1996; *Herbaut et al.*, 1997].

2. the Liguro-Provençal Current, that represents the northern branch of the cyclonic circulation of the western Mediterranean Basin. The core of this along-slope current is about several hundreds meters thick and is primarily composed of Modified Atlantic Water, from the surface down to 100–150 m depth, and Levantine Intermediate Water.

3. fresh waters from the Rhône river, whose plume sometimes extends over a hundred kilometers [*Estournel et al.*, 1997]. The dispersion of the riverine waters tends to reduce the density of the coastal water.

[7] The oceanographical part of the FETCH experiment, that gathered currentmeters, hydrological and meteorological data during one month, aims at analyzing the effect of these different forcings, particularly the effect of winds, on the Gulf of Lion circulation. The first period of the cruise is characterized by typical unstratified winter conditions and intense N-NW winds. The measured currents suggest the presence of large current cells on the shelf but the temporal fluctuations of the wind does not permit to confirm their persistence. The SYMPHONIE model is used to reconstruct the oceanic circulation and its temporal evolution. The results are used to emphasize the mechanisms, which are responsible of the observed circulation patterns.

[8] The first part of this article describes the experiment, and presents the characteristics of the hydrodynamic model and meteorological forcings (wind and heat fluxes). In the second part, the currentmeters and hydrological observations are contrasted with the simulation in order to validate the model. In the final part, the role of the wind curl on mesoscale shelf circulation is highlighted.

2. Material and Methods

2.1. Field Observations

[9] The first leg of FETCH cruise took place from 13 March to 29 March 1998. A network of 20 hydrological stations was performed twice. The first survey occurred between 13 March and 19 March, and the second survey occurred between 22 March and 26 March. Additional stations were performed on 20 and 21 March along cross-shelf transects, which were dedicated to precisely measure the air-sea exchanges [*Hauser et al.*, 2003]. Current and hydrological data were continuously collected along the ship's track.

2.1.1. Current Data

[10] Current profiles are collected with an acoustic Doppler current profiler (ADCP RDI Broad Band VM300) mounted on the hull of the R/V L'Atalante. Currents are measured for 50 bins of 4 m length each. The shallowest reliable measurements is at 10 m depth and the deepest is at 150 m. For water depths less than 150 m, the deepest reliable bin is at 85% of the water depth. Current profiles are estimated and recorded every 2 min during the survey. The horizontal velocities are converted into an orthogonal Earth coordinate system. The Earth coordinates velocity components are the east-west velocity (positive eastward) and the north-south velocity (positive northward).

[11] Since the bottom tracking mode is disabled, the translational motion of the ship is inferred solely from the

differential-GPS positioning of the ship. The SIMRAD echo sounder records and the ADCP backscatter intensity are used to infer the seafloor depth and the real depth range of the velocity profiles. The water tracking calibration methods described by *Joyce* [1989] and *Pollard and Read* [1989] are performed to correct the velocity components from misalignment of the transducers head with respect to the ship's axes. We use the reference layer velocities before and after sharp turns of the ship as well as accelerations and decelerations of the ship at stations. The reference layer velocities is obtained by averaging over several bins covering the 10–86 m depth range.

[12] For the present study, profiles are averaged spatially along the ship's track over approximately 2000 m traveled distances. The detailed description of the raw data analysis is presented by *Durrieu de Madron* [1999].

2.1.2. Hydrological Data

[13] Hydrological casts are made using a Seabird 9/11 Plus CTD probe between the surface and few meters above the bottom. The data are recorded into 24 Hz time series during the data acquisition. After filtering and validation, the downcast portion of each cast is pressure-averaged and sequenced into 1 decibar pressure intervals [*Taillez et al.*, 1999].

[14] A SIS-CTD 1000 thermosalinograph is used to measure the near surface (~3m deep) temperature and conductivity along the ship's track. The sampling period is set to 10 seconds. These parameters are corrected from the warming of the water within the circuit linking the water input, located at the bow of the ship, and the instrument cell [*Taillez et al.*, 1999].

[15] Temperature is expressed according to the ITS-90 scale. Salinity and density are derived according to the 1978 practical salinity scale and the 1980 equation of state for seawater respectively [*Millero and Poisson*, 1981].

2.1.3. Sea Surface Temperature

[16] Daily sea surface temperature (SST) fields are derived from Advanced Very High Resolution Radiometer (AVHRR) satellite data provided by the SATMOS center. They are composite images resulting from various satellites passages. They are not calibrated versus field measurements collected during the FETCH cruise, and are thus used only qualitatively to describe the major superficial temperature structures.

2.1.4. Meteorological Fluxes

[17] One of the objectives of the FETCH experiment was to improve the parameterization of turbulent fluxes at the air-sea interface. *Hauser et al.* [2003] compared different calculation methods of these turbulent fluxes using ship-borne measurements. In the present study, we use the fluxes computed with the dissipation method to correct the output of a meteorological model used to force the oceanic model at the sea surface.

2.2. Numerical Model

2.2.1. Model Specifications

[18] The SYMPHONIE model has been described in details by *Auclair et al.* [2000a, 2000b]. This model was used earlier to describe the dynamics of the Rhône river plume and its response to the wind [*Estournel et al.*, 1997; *Marsaleix et al.*, 1998; *Estournel et al.*, 2001]. It is a three-dimensional (3-D) primitive equations, sigma coordinate model with a free surface explicitly calculated by decomposition of the model equations into internal and external modes as proposed by *Blumberg and Mellor* [1987]. Vertical turbulence is estimated using the second-order closure scheme of *Gaspar et al.* [1990], with a prognostic equation for the turbulent kinetic energy and an algebraic formulation of the mixing and dissipation lengths. The advection scheme of *Beckers* [1995] is used for temperature and salinity. The model has 25 vertical levels, of which 15 are irregularly distributed on the first 300 meters of the offshore water column following *Auclair et al.* [2000a]. For a 100 m deep water column, six vertical levels are distributed on the first ten meters under the surface. The horizontal mesh is 3.3 km. The viscosity used in the Laplacian horizontal diffusion term is set to 10 $m^2\ s^{-1}$ on the continental shelf and then progressively increased up to 40 $m^2\ s^{-1}$ in a boundary sponge layer in order to damp potential numerical instabilities generated by the open boundary conditions scheme. Figure 1 shows the modeled domain. Its main open boundary is parallel to the continental slope.

2.2.2. Boundary Conditions and Initialization

[19] The near-bottom friction is parameterized by a logarithmic law with a roughness length of 10^{-4} m. The boundary conditions at the surface are standard: the momentum flux is equal to the wind stress, the heat flux is the resultant of the atmospheric fluxes (sensible and latent heat fluxes) and radiative fluxes (short and long wavelengths). The penetration of solar flux in the superficial layers decreases exponentially with depth. The salinity flux is calculated from the evaporation (precipitations are null for the period considered). The flux of turbulent kinetic energy at the surface is based on a balance between the production and dissipation terms [*Gaspar et al.*, 1990].

[20] The freshwater supply by the major rivers (Rhône, Hérault, Aude and Orb) is taken into account (Data from the Compagnie Nationale du Rhône and the Directions Départementales de l'Équipement). The Rhône river discharges represent more than 90% of the total freshwater inputs for the period considered. The boundary condition at the river mouth is prescribed from the daily measurements of the discharge following *Estournel et al.* [2001]. The average Rhône discharge over the duration of the simulation is about 970 $m^3\ s^{-1}$, which is lower than the mean annual value (1670 $m^3\ s^{-1}$).

[21] A characteristic radiation condition is applied at the open lateral boundaries [*Oey and Chen*, 1992]:

$$U - U_f = \pm\sqrt{gH}\left(\eta - \eta_f\right)$$

where η is the free surface elevation, U is the component of the transport normal to the boundary and the index f refers to the large scale fields forcing. An upstream condition for temperature and salinity implies that large scale fields, T_f and S_f, are advected into the simulated domain under inflow conditions. The large scale field considered as constant during the simulation period is also applied over the whole grid at $t = t_0$ as an initial state of the presented simulation. The determination of the latter is detailed in Appendix A. The initial fields allow to represent the mean characteristics, observed during the first leg of FETCH, of the large scale circulation (i.e., the Liguro-Provençal alongslope current). For water depth lower than 100 m, the initial currents are near zero and the temperature and salinity fields are quasi

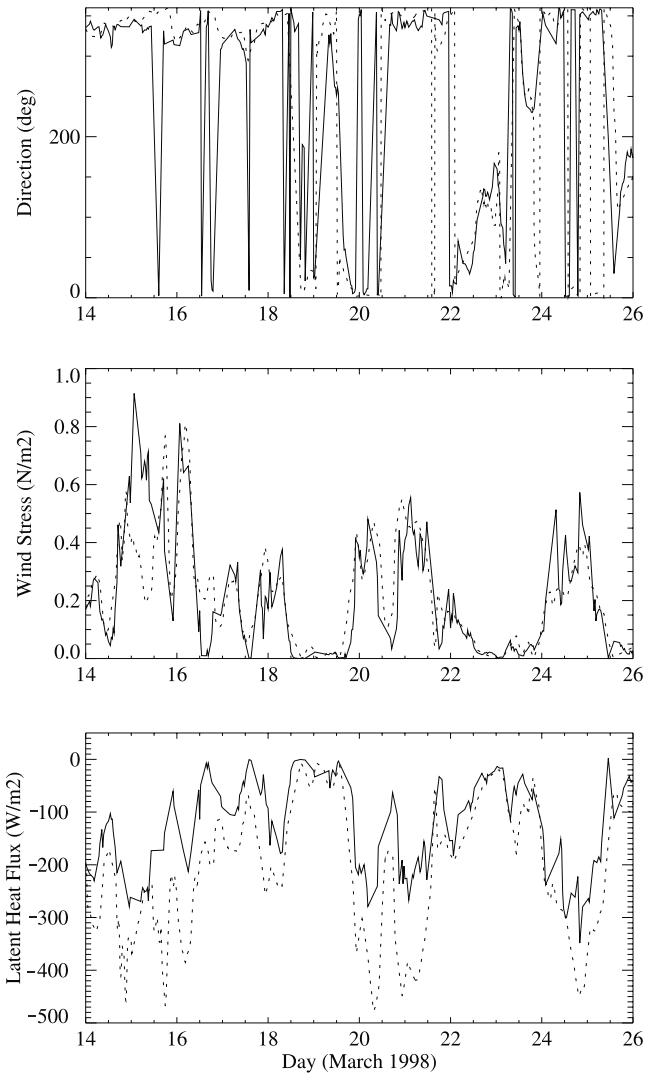

Figure 2. Comparison of the wind stress (direction and amplitude) and latent heat flux measured on board of the R/V Atalante (solid line) and simulated from the Aladin meteorological model (dotted line) along the ship's track.

homogeneous both horizontally and vertically. The simulation starts at t_0 corresponding to 6 March, about 8 days before the first observations. Sensitivity studies to the spin-up duration and the different comparisons between simulated and observed fields indicate that this period of 8 days looks long enough to allow the wind driven circulation and the Rhône plume to settle on the shelf.

2.3. Analyses of Meteorological Forcings

[22] The model is forced at the surface by the wind stress and the heat fluxes. The fluxes measured on the ship during the experiment are not sufficient to precisely characterize the spatial and temporal variability of the surface fluxes necessary to correctly model the mesoscale circulation on the continental shelf. Instead of these ship-borne data, we use data from the high resolution ($0.1 \times 0.1°$) weather-forecast model Aladin from Météo-France. Surface fluxes are available every 3 hours and are integrated over this duration. The field of each specific flux at a given time is interpolated on the grid of the model. For each time step of the model, a linear interpolation is performed between two successive fields.

[23] A comparison of the wind stress measured along the ship's track and the corresponding values from the Aladin model is presented in Figure 2. The Aladin wind stress does not present any systematic bias with respect to the field observations. With the exception of a few periods like 15 March, the Aladin outputs correctly reproduce the variations of the wind intensity and direction.

[24] This comparison is also carried out for the different components of the heat flux (sensible, latent, short and long waves fluxes). During periods of N-NW winds, latent heat flux, which induces a strong heat loss from the sea to the atmosphere, has a major influence. A comparison of the Aladin latent heat fluxes with the observations reveals that the Aladin model overestimates the heat flux, especially when the fluxes are intense (Figure 2). In order to obtain a more appropriate forcing for the oceanic model, we adjusted statistically the Aladin fluxes to the observations (Figure 3). The least squares fittings yields the following relations:

$$LE^* = 0.79\ LE + 45$$

$$H^* = H - 15$$

$$F_{ir}^* = F_{ir} + 30$$

$$F_{sol}^* = F_{sol}$$

$$\tau^* = \tau$$

where, LE, H, F_{ir}, F_{sol} are the latent, sensible, net long wavelength, solar heat fluxes and the wind stress from the Aladin model whereas the asterisks refer to the corrected flux values used in the oceanic model. The Figure 4a presents the temporal variation of the corrected nonsolar flux ($LE^* + H^* + F_{ir}^*$) and wind stress averaged on the domain.

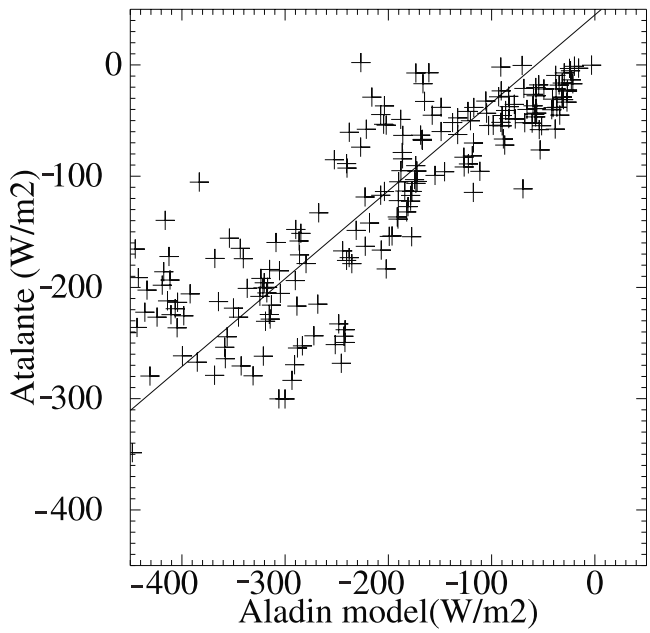

Figure 3. Comparison of the latent heat measured on board of the R/V Atalante and simulated from the Aladin meteorological model along the ship's track. The straight line indicates the least squares regression used to correct the data from the Aladin model.

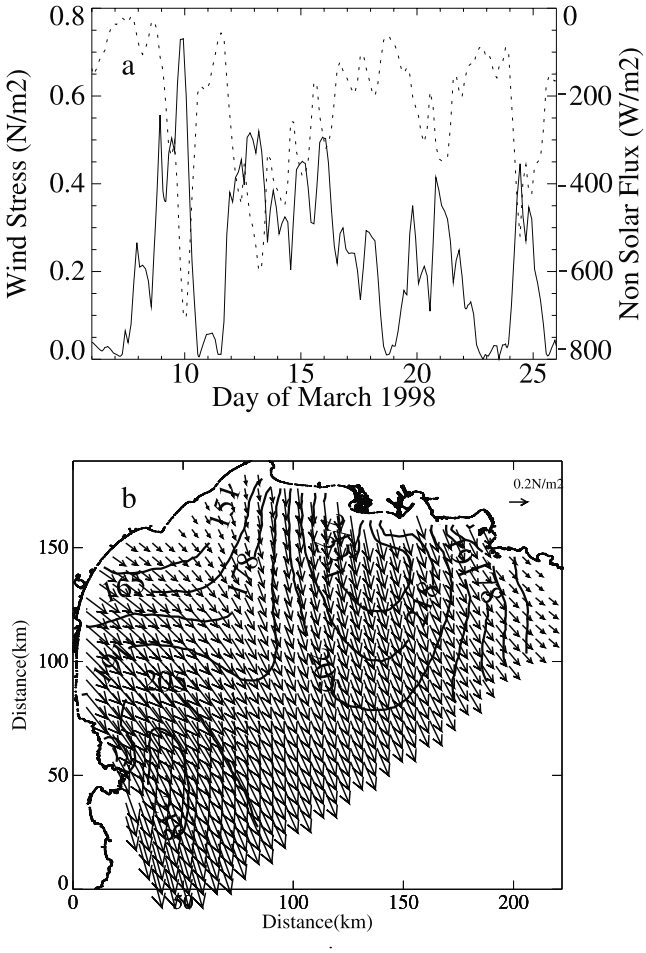

Figure 4. (a) Temporal variation of the wind stress (solid line) and the nonsolar heat flux (dotted line) averaged over the model's domain. (b) Spatial distribution of the wind stress (arrows) and the nonsolar heat flux (annotated contours) averaged over the modelled period (6–26 March 1998).

For clarity of the figure, the solar flux is not represented. It has a daily mean value of about 200 W m^{-2}. The heat budget at the surface is thus in deficit. Given an average water layer thickness of 100 m, this heat loss produces over the period from 6 March to 26 March a net cooling of 0.12°C. Likewise, if one considers only the 10 to 16 March period, which includes two gales, the cooling reaches 0.38°C.

[25] The Figure 4b presents the spatial distribution of the nonsolar flux and wind stress averaged over the modeled period (6–26 March). The spatial structure of the wind stress shows two maxima, in the northern and the southwestern parts of the shelf, corresponding to the paths of the Mistral and Tramontane. The maximum values of the wind stress are about 5 times higher than the minimum values. The maximum intensity of the wind is observed near the Cape Creus at the southwestern tip of the gulf. The strongest heat loss is observed in the northern part of the gulf, associated to the cold and dry Mistral.

3. Comparison Between Observations and Model

[26] We present here an assortment of comparisons between the model's simulations of the temperature, salinity and velocity fields and the observed fields. We attempt to show that the model reproduces the major hydrological and circulation characteristics.

3.1. Horizontal Distribution of Surface Temperature and Salinity

3.1.1. Observed Surface Temperature and Salinity

[27] AVHRR sea surface temperature between 14 March and 21 March (Figures 5a–5c) highlights the superficial thermal structures and their temporal variability over the whole Gulf. The image of 14 March evidences the warm path of the Liguro-Provençal Current that roughly follows the continental slope. The slope current intrudes on the shelf at the eastern part of the gulf. A tongue of warm water penetrates onto the shelf at the longitude of Sète (~3°40′E) isolating two regions of colder water south of the Camargue and along the Languedoc-Roussillon coast. During the next week, the intrusion at the eastern part of the shelf develops as a westerwards propagating meander and the tongue of warmer water rapidly fades.

[28] Surface salinity field is described from thermosalinograph data (Figure 6a) obtained during the first survey (14–19 March). A map of these data shows the salinity field, and illustrates the freshest waters south of the Rhône river mouth and a dilution area extending toward the W/SW up to the longitude of Sète (3°40′E).

3.1.2. Simulated Surface Temperature and Salinity

[29] Figures 5d–5f show the simulated surface temperature on 14, 17, and 21 March at 0H. The path of the Liguro-Provençal Current is clearly identified by the warm temperature strip that cools downstream. The position of the front separating the colder coastal water from the slope water is generally well defined. The northward intrusion of the slope water onto the shelf at the latitude of Sète, observed on the SST, is also clearly seen in the model outputs. The model also reproduces the cold water region south of the Camargue observed on SST, in particular that of 17 March, though the contrast with neighboring waters seems stronger than in reality. It is noteworthy that the temperature minimum south the Camargue coincides with the region of maximum heat loss (Figure 4b). However, the model does not reproduce the cold water band observed along the Roussillon coast. The heat loss in this zone is minimal (Figure 4b) and it is likely that their formation occurred prior to the initialization of the model.

[30] The modeled surface salinity along the ship's track is shown in Figure 6b. The comparison with the observations (Figure 6a) illustrates that the dilution area of the freshwater coming from the Rhône river is well located, though salinity values are overestimated in the distal part of the dilution area. The instantaneous salinity (not presented here) and temperature fields from the model indicate that the dilution area expands in the southwest direction, hugging and overlapping the eastern side of the tongue of cold water that also spreads south-southwest off the Camargue coast (Figures 5d–5f).

3.2. Vertical Distribution of Temperature, Salinity, and Density

3.2.1. Observed Vertical Distributions

[31] During wintertime, the surface layer between the surface and 150 m depth is rather homogeneous. However, in small areas, variations of temperature and salinity related to

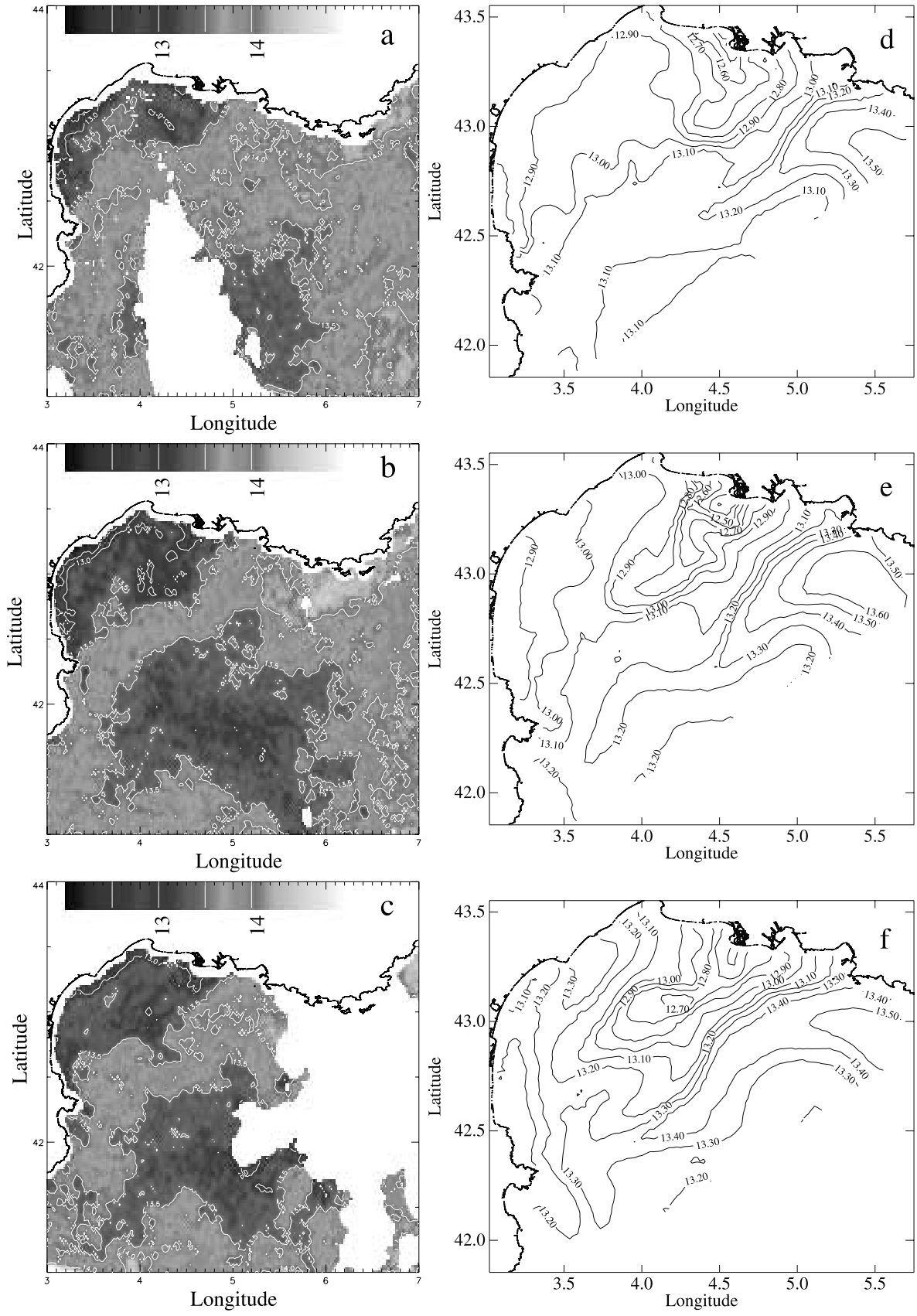

Figure 5. Comparison of the observed and simulated sea surface temperatures. AVHRR SST images for the 14 March 1998 (a), 17 March 1998 (b) and 21 March 1998 (c). Simulated SST distribution for the 14 March 1998 (d), 17 March 1998 (e) and 21 March 1998 (f). See color version of this figure at back of this issue.

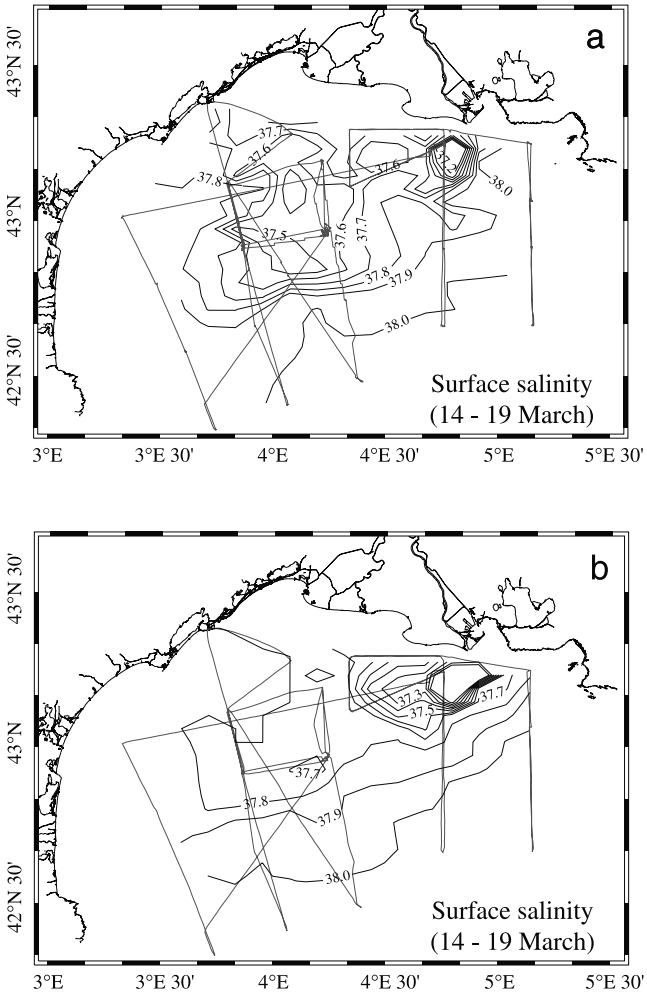

Figure 6. Comparison of the observed and simulated sea surface salinity. (a) Map of surface salinity measured along the ship's track between the 14 and 19 March 1998. (b) Map of surface salinity simulated by the model along the ship's track between the 14 and 19 March 1998.

the interleaving of water of different characteristics and origin are observed. This confrontation of waters is clearly visible on the FETCH02 cross-shelf section performed on 21 March in the central part of the gulf (~4°15′E) (Figures 7a–7c). This section shows that the layer influenced by the dilution of the Rhône river plume appears as a lower salinity layer between 40 and 60 m thick. It is bordered by a narrow band of homogeneous water near the coast and the warmer and saltier slope water. Near the bottom, the water on the inner- and midshelf resembles the slope water at 80 m depth, but are separated by a core of cold and less saline water.

[32] The mapping of the temperature and salinity field at 20 meter above the bottom (Figure 8a and 8b) defines the limit of these two water masses. Though this altitude is relatively distant from the seafloor, it allows to preserve the largest number of stations for mapping. Thus, the cold and less saline water forms a cell south of the Camargue. The warmer and saltier water extends on the outer- and midshelf between the latter section and about 3°40′E. The presence, at some stations, of salinity up to 38 very near the bottom (data not shown) confirms that this water is upwelled from the slope. The presence of warm and salty waters east of the Rhône also attests the intrusion near the bottom of slope water onto the shelf similar to that observed for the surface layer with the SST.

3.2.2. Simulated Vertical Distributions

[33] Figure 8c and 8d presents the temperature and salinity fields on the first level of the model above the bottom. The outputs are given for the 17 March, which corresponds to the midterm of the first survey (14–19 March 1998). The modeled structures clearly illustrate the intrusion of slope water onto the shelf east of the Rhône, and also on the western part of the shelf. The presence of a tongue of cold and less saline water offshore of the Camargue with a clear cross-shelf frontal zone is also evidenced. However, the model shows the southwestward spreading of this water more important than that inferred from the observations.

[34] The Figures 7d–7f displays the modeled vertical hydrological structure on a cross-shelf section around 4°E20′, close to the FETCH02 section. These outputs show the dilution layer of the Rhône river plume on the midshelf, a core of cold water near the bottom, and the upwelling of warm and salty slope water onto the outer shelf. The modeled temperature on the inner shelf is slightly colder than the observed temperature. This discrepancy probably relates to the position of the section, since Figure 8c indicates that the temperature near the coast gets warmer west of the section.

3.3. Horizontal and Vertical Distributions of the Currents

3.3.1. Observed Currents

[35] The horizontal circulation patterns observed from the shipborne ADCP are represented for the two surveys. As current profiles are rather homogeneous over most of the shelf, the current fields at 30 m depth (Figure 9) give a reliable and complete picture of the main current patterns on the shelf. The cyclonic flow of the Liguro-Provençal current is well identified at the southern end of the cross-slope sections for the two surveys. The core of the current, centered above the 1000 m isobath, is about 25 km wide and shows maximum velocities between 40 and 50 cm s^{-1}. On the western part of the slope, a narrow eastward flowing counter current borders the inner side of the current. The circulation of the shelf is more complex and the currents reach maximum speed of 30 cm s^{-1}. It is primarily directed to the west on the outer shelf and to the east on the inner shelf. For the first survey, the rotation of the currents along the cross-shelf and along-shelf sections centered around 4°E and 43°N suggests the presence of an anticyclonic eddy over the central part of the shelf, whereas for the second survey the anticyclonic circulation extends over most of the shelf.

[36] The vertical structure of the current for the cross-shelf section performed on 21 March in the central part of the gulf (~4°15′E) is presented in Figure 10a. The Liguro-Provençal Current appears between stations 34 and 35 as a core of strong currents heading to the southwest. The current intensity within the core decreases from about 30 cm s^{-1} near the surface to about 15 cm s^{-1} at 100 m depth. The layer of freshwater influence that extends from the midshelf to the upper slope (stations 39 to 35) moves

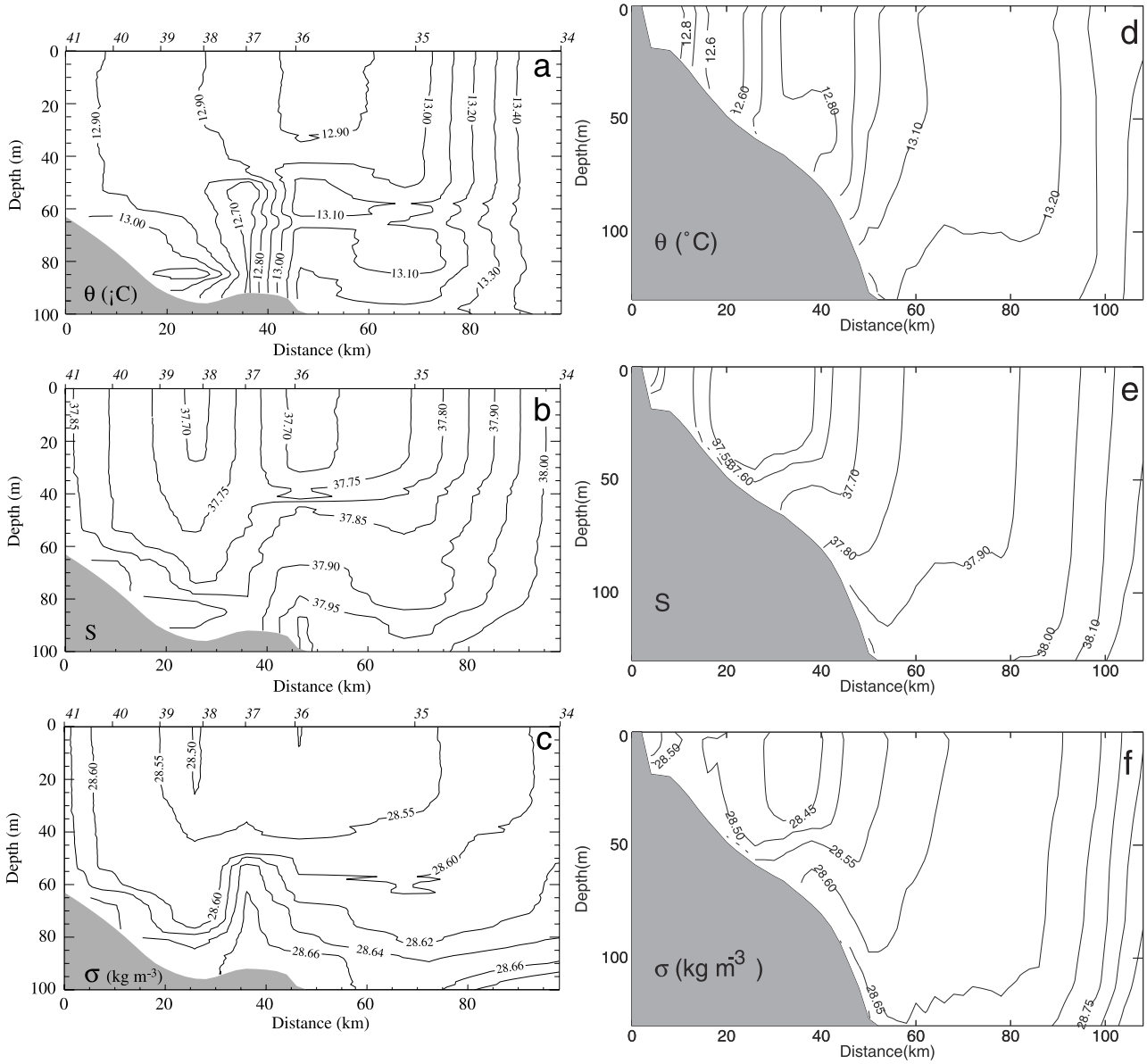

Figure 7. Comparison of the observed and simulated hydrological structures on a cross-shelf vertical section. Observed distribution of potential temperature (a), salinity (b) and potential density anomaly (c) on the FETCH02 section performed on the 21 March 1998 around 4°E15′ of longitude. Simulated distribution of potential temperature (d), salinity (e) and potential density anomaly (f) on a cross-shelf section performed on the 17 March 1998 around 4°E15′ of longitude.

westward with a mean velocity of about 15 cm s^{-1}. Below that layer, the currents are slower (<5 cm s^{-1}) and moves in different directions. The narrow core of cold water observed at station 37 moves toward the west. The currents on the upper slope are directed to the northwest, i.e., they present a cross-slope component inducing the upwelling of slope water on the shelf. A narrow eastward flowing current, associated to the strong tilting of the isopycnals (Figure 7c), is observed at the shelfbreak (station 36). Finally the barotropic coastal jet with velocity up to 30 cm s^{-1} skirts the shore to the east.

3.3.2. Simulated Currents

[37] Figures 9c and 9d show the simulated currents along the ship's track for the two surveys. The position and the intensity of the Liguro-Provençal along the slope agree with the observations. The eastward flowing counter current on the slope is not reproduced, but a significant slowing down of the westward flowing flow appears above the upper slope. The comparison on the shelf is more difficult because there is a strong variability in both the observed and simulated currents. Model results nevertheless reproduce the intensity and the direction of the major patterns on the outer shelf and near the coast. Figure 10b presents the zonal and meridional currents on a cross-shelf section close to the FETCH02 section. Similarities between the simulated and observed currents exist, although quantitative discrepancies are obvious. From the coast to the open sea and below the surface Ekman layer, not described by the observations, one

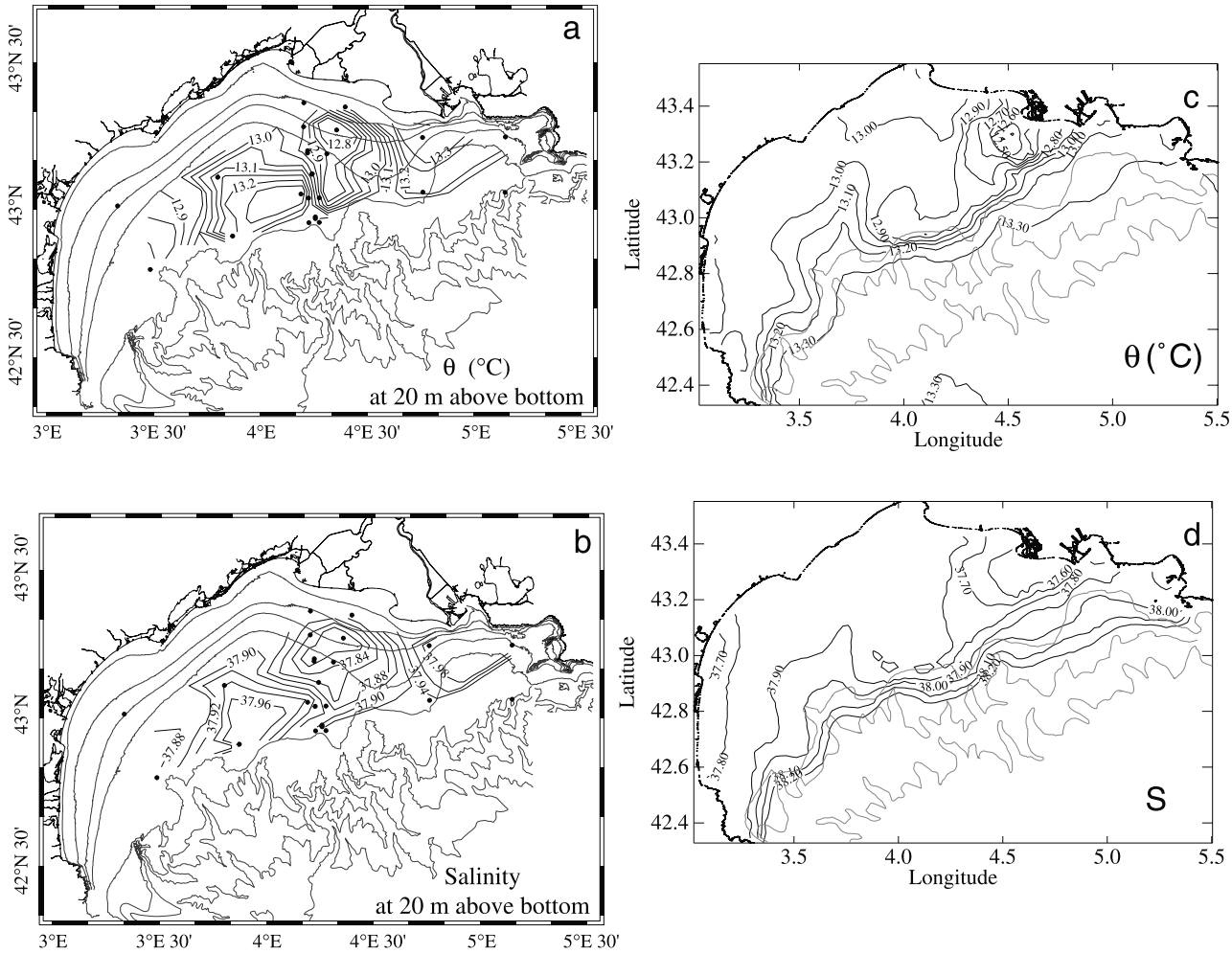

Figure 8. Comparison of the observed and simulated temperature and salinity near the bottom. Map of near bottom (20 mab) potential temperature (a) and salinity (b) measured along the ship's track between the 14 and 21 March 1998. Map of near bottom potential temperature (c) and salinity (d) simulated by the model for the 17 March 1998.

finds the southwestward flowing core of the Liguro-Provençal current with intensities comparable to the observations. At the shelfbreak, the slope water tends to upwell on the shelf in accordance with the observations. The eastward flow on the slope is also present, but is slightly deeper than the observed one. On the outer shelf, the southwestward flow is correctly reproduced whereas the eastward coastal jet is correctly located but is weaker than in reality.

3.4. Conclusions on the Data/Model Comparison

[38] Qualitatively, the simulation reproduces the major hydrological and circulation features observed during the cruise. Quantitatively, it is unrealistic to expect a perfect agreement between the model and the observations given the crude initialization of the model. Despite the brevity of the simulation, it is worth to note that the atmospheric forcing and the freshwater inputs produce temperature and salinity fields close to the observed fields.

[39] Some deviations between the model and the observations can probably be explained by the uncertainty in surface fluxes (example of the storm of 15 March missed by the atmospheric model) and in the initial state of the model especially the temperature field on the shelf. For instance, cold waters localized along the western coast on the satellite SST are not represented by the model. If we assume that the spatial distribution of the atmospheric fluxes used to force the model are not questionable, an explanation could be that the residence time of this water body exceeds the duration of the simulation (i.e., this water body was probably present before the beginning of the simulation and was not included in the initial temperature field). It is difficult to quantify the relative importance of initial and forcing conditions on the forecasting errors due to the lack of observations on the atmospheric fluxes during the spin-up period and on the density field at the initial state (only a SST field on 3 March is available before the one of 14 March; Figure 5a). For lack of in situ data allowing to correct the initialization of the model, an assimilation of the SST data in the coastal zone would permit to minimize this error. Salinities in the distal part of the dilution area are overestimated, especially for the first period of simulation (14–19 March, Figure 6). The

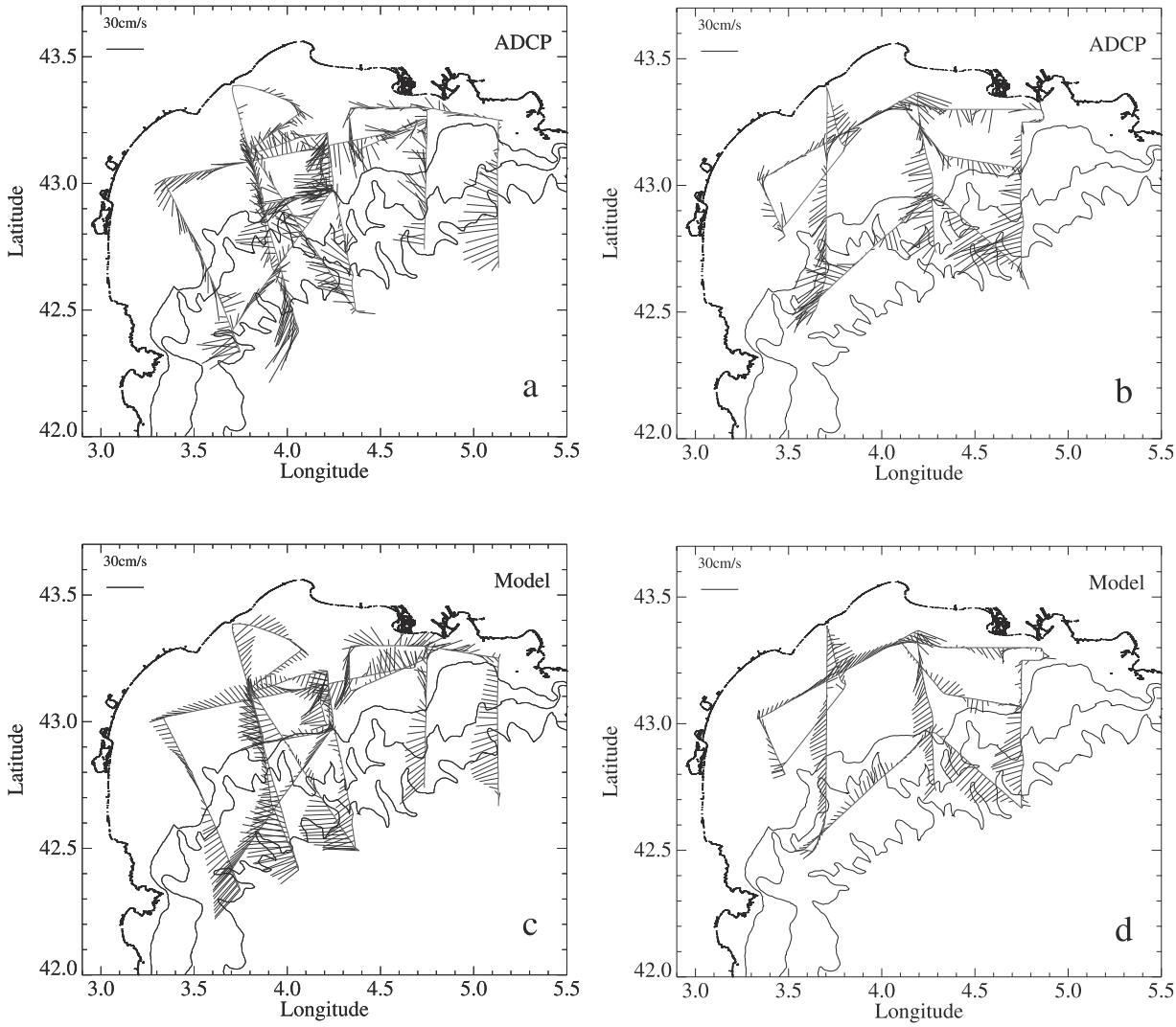

Figure 9. Comparison of the observed and simulated horizontal distribution of the currents. Observed currents at 30 m depth along the ship's track for the first survey (14–19 March 1998) (a), and the second survey (22–26 March 1998) (b). Simulated currents at 30 m depth along the ship's track for the first survey (14–19 March 1998) (c), and the second survey (22–26 March 1998) (d).

observed differences between the simulated and in-situ salinity fields may be due to various numerical problems including an insufficient spin-up duration, a coarse grid mesh, and/or too much diffusion produced by the advection scheme.

[40] The initialization method of the general circulation is based on simple concepts. However, it allows us to accurately reproduce the position and vertical structure of the Liguro-Provençal and its interaction with the continental slope. The narrow eastward current linked to the tilting of isopycnals at the shelf break is only partially reconstituted by the model. This inconsistency could be attributed either to the short spinning period of the model, that does not reproduce correctly the ascent of isopycnal. It is also probable that the grid mesh size and the horizontal diffusion are too large to describe correctly this small scale structure. The influence of the shelf topography should be also investigated insofar as the tilting of isopycnals and the position of the front between the shelf and slope waters could be related to the presence of a topographical bump located on the external shelf near 4°E (Figures 1 and 7c). The model bathymetry is not enough accurate to take correctly into account the local consequences of these topographical features on the density field. On the shelf, the large scale structures of the circulation are rather well reproduced but the mixing of the spatial and temporal variability in the data makes a finer analysis difficult.

[41] In conclusion, the present simulation seems close enough to the observations to serve as a base for the interpretation of the system, then allow us to widen this interpretation in a more general frame.

4. Analysis of the Driving Mechanisms on the Shelf Circulation and Their Implication

[42] The observations and the simulations emphasize the various processes that take place during March 1998 in the Gulf of Lion, in particular the intrusion/upwelling of slope

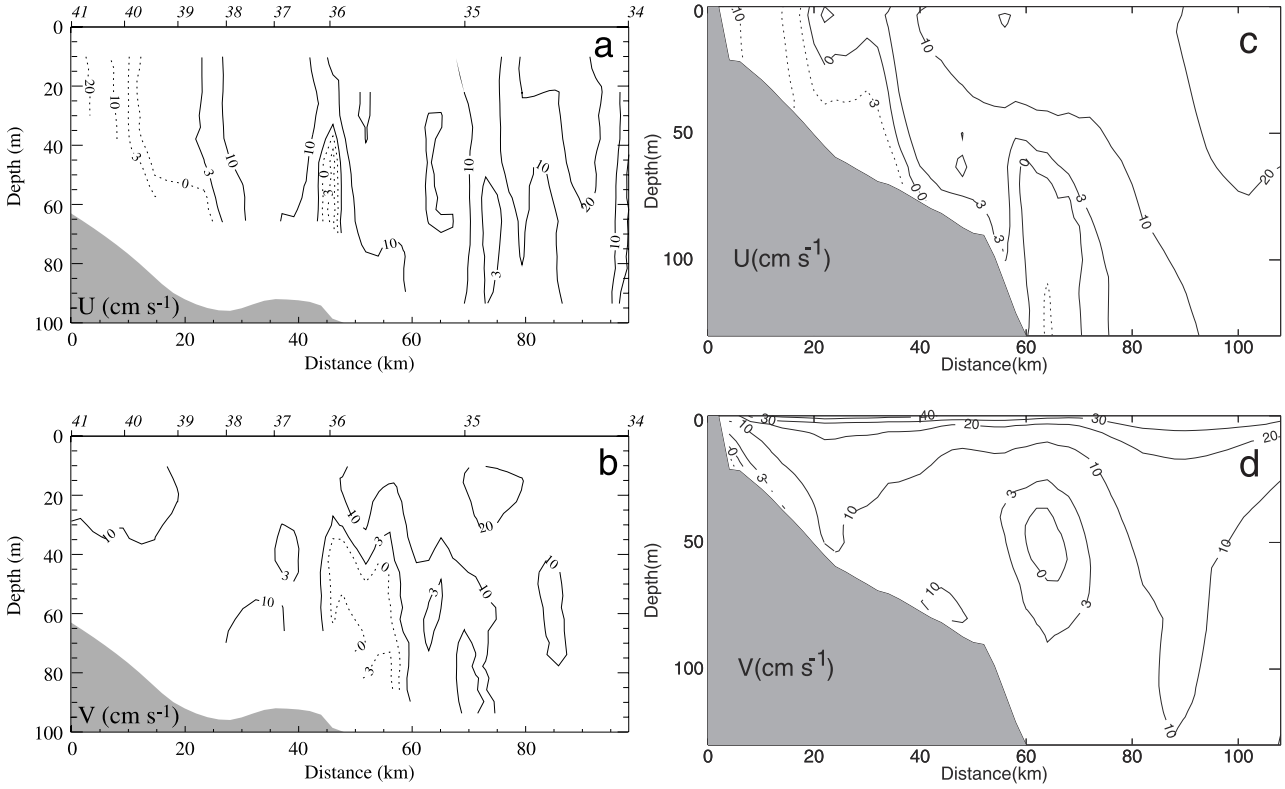

Figure 10. Comparison of the observed and simulated distribution of the currents on a cross-shelf vertical section. Observed distribution of zonal (a), and meridional (b) currents on the FETCH02 section performed on the 21 March 1998 around 4°E15′ of longitude. Simulated distribution of zonal (a), and meridional (b) currents on the FETCH02 section performed on the 21 March 1998 around 4°E15′ of longitude. Solid isolines correspond to negative values and dashed isolines correspond to positive values.

water onto the shelf, the downwelling of cold dense water and the relatively complex circulation on the shelf. The validation of the model in the previous paragraph lets us to have some confidence in the simulated circulation patterns and hydrological structures. By procuring a detailed description of the circulation at any time, it allows to analyze the respective effect of dominant physical forcing (wind stress, heat flux, freshwater).

4.1. Effect of Wind on the Appearance of Eddies on the Shelf

[43] The observed currents on the continental shelf (Figures 9a and 9b) indicate the presence of eddy structures whose extension is variable. During the first period (Figure 9a), an anticyclonic eddy—centered on 4°E and of about 50 km wide—occupies the northern part of the gulf whereas the currents on its western part seem rather directed southward. Figure 9b also indicates the presence of an anticyclonic eddy but extending over most of the shelf. However, the incomplete spatial coverage and the duration of the surveys unable us to confirm the existence of these structures as well as their lifetime.

[44] The model is used to solve these uncertainties and to assess the effect of the wind. Figure 11 presents two snapshots of the depth-averaged circulation that are representative of the observed conditions during the two surveys. The first period (13–18 March, Figure 11b) is characterized by the coexistence of the Mistral blowing over the eastern half of the gulf and the Tramontane blowing over the western half. During the second period (19–26 March, Figure 11d), the Mistral persists while the Tramontane weakens yielding a more unidirectional wind field. The circulation obtained for both situations corroborates the observations (Figures 9a and 9b). For the first period (Figure 11a), the shelf circulation is dominated by an anticyclonic eddy in the central part of the shelf and a cyclonic circulation with a strong southward coastal current in the western part of the shelf. For the second period (Figure 11c), the anticyclonic circulation extends over the whole shelf inducing a reversal of the coastal current along the western coast.

[45] A sensitivity study of the oceanic circulation to the wind, river discharge and heat flux shows that the strength, direction and spatial structure of the wind mainly affect the circulation. Four academic simulations with simplified wind fields illustrate the role of the wind direction and curl (Figure 12). The currents are averaged vertically and over one inertial period following three days of constant forcing (wind stress = 0.5 N m^{-2}). This duration is sufficient to obtain a quasi steady state circulation. Because of the crescent-shape of the gulf, the circulation in some areas is particularly sensitive to the wind direction. For a spatially homogeneous northwestern wind (Figure 12a), the entire shelf region between Cape Creus and the Rhône is affected by upwelling due to a depression of the sea surface near the coast inducing a northeastward circulation. For an homogeneous northern wind (Figure 12b), the situation is more complex: (i) the

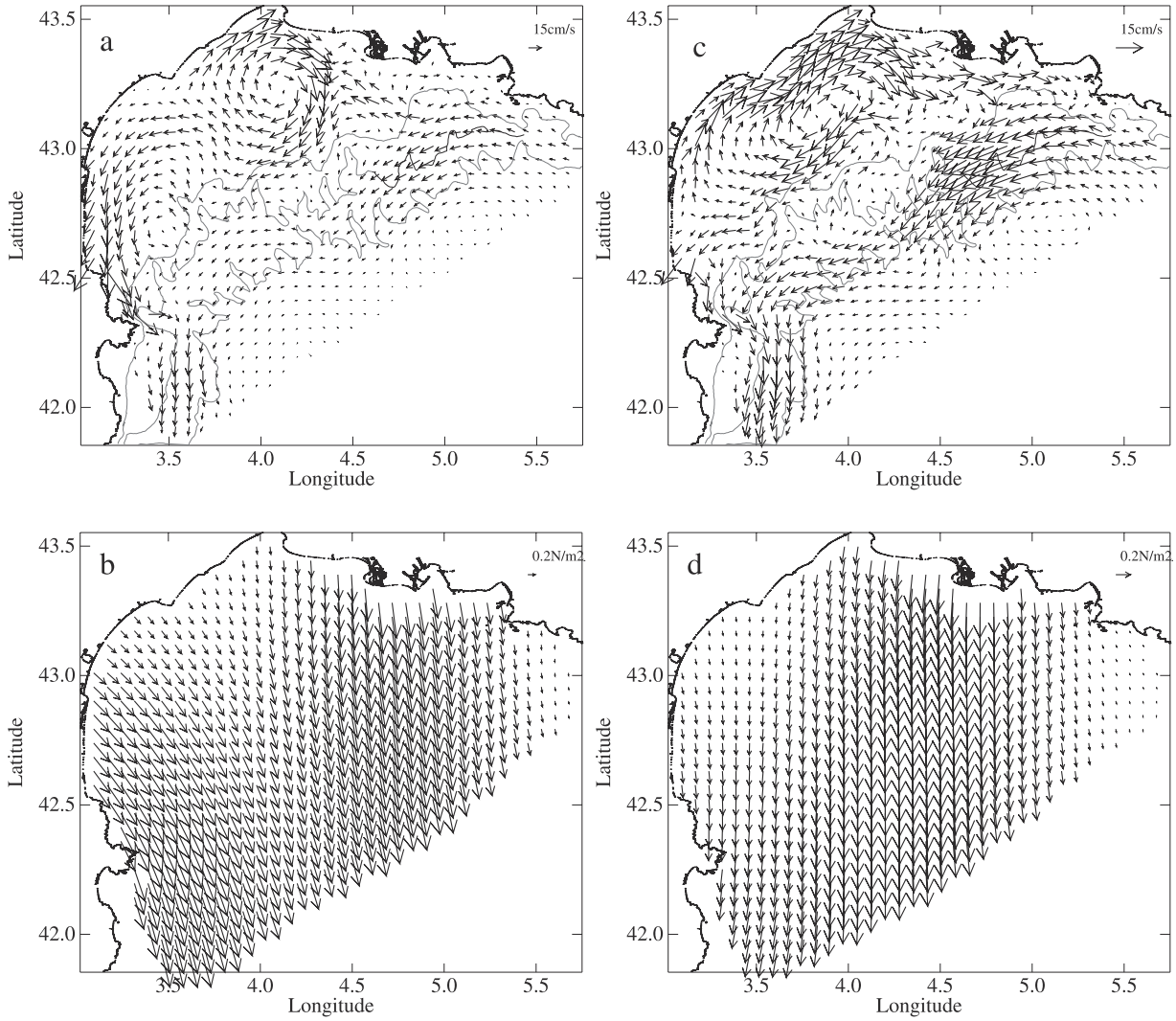

Figure 11. Depth-averaged current field for the 16 March 1998 (a) and 20 March 1998 (c). Wind fields for the 16 March 1998 (b) and 20 March 1998 (d).

western coast is favorable to a downwelling circulation: due to the vanishing cross-shore component of the Ekman transport at the coast, an equilibrium is achieved through dissipation effects, resulting in an enhanced southward coastal jet (ii) the northern coast, rather favorable to upwelling, shows no significant transport because of the opposition between the westward Ekman transport and the eastward geostrophic current [*Csanady*, 1982]. Finally the transition area between the upwelling and the downwelling circulations is characterized by a strong divergence which is compensated by an anticyclonic circulation on the inner shelf.

[46] In the next two simulations, we assess the influence of the curl of the Mistral and Tramontane winds (Figures 12c and 12d). For that purpose, we impose a wind stress of 0.5 N m^{-2} along the axis of both winds determined from the wind field depicted in Figure 11b. The wind stress decreases linearly over a distance of 100 km on both sides of the maximum wind axis. The comparison with the previous simulations, that consider homogeneous wind fields, reveals that the shelf circulation is closely linked to the wind curl. For example, in the case of the Tramontane (Figure 12c), the circulation on the western part of the shelf is inverted with regard to the case of a uniform Tramontane (Figure 12a). The wind curl induces an anticyclonic eddy circulation (Figure 12d) on most of the shelf in the case of the Mistral (negative wind curl) and a cyclonic circulation in the western half of the shelf in the case of the Tramontane (positive wind curl).

[47] To finish this sensitivity study, we look at the constraint exerted by the topography of the continental shelf on the coastal circulation. For that purpose, we perform a simulation identical to that illustrated on Figure 12d except for the topography characterized by a 100m deep flat bottom on the shelf (Figure 13). One can see that the main characteristics of the circulation are little influenced by the shelf topography thus confirming the determining role of the wind field. Local variations are nevertheless observed, e.g. for the flat shelf case, the anticyclonic eddy penetrates farther eastward due to the deepening of the shelf which is relatively narrow south of the Rhône delta. In fact, the determining effect of topography is

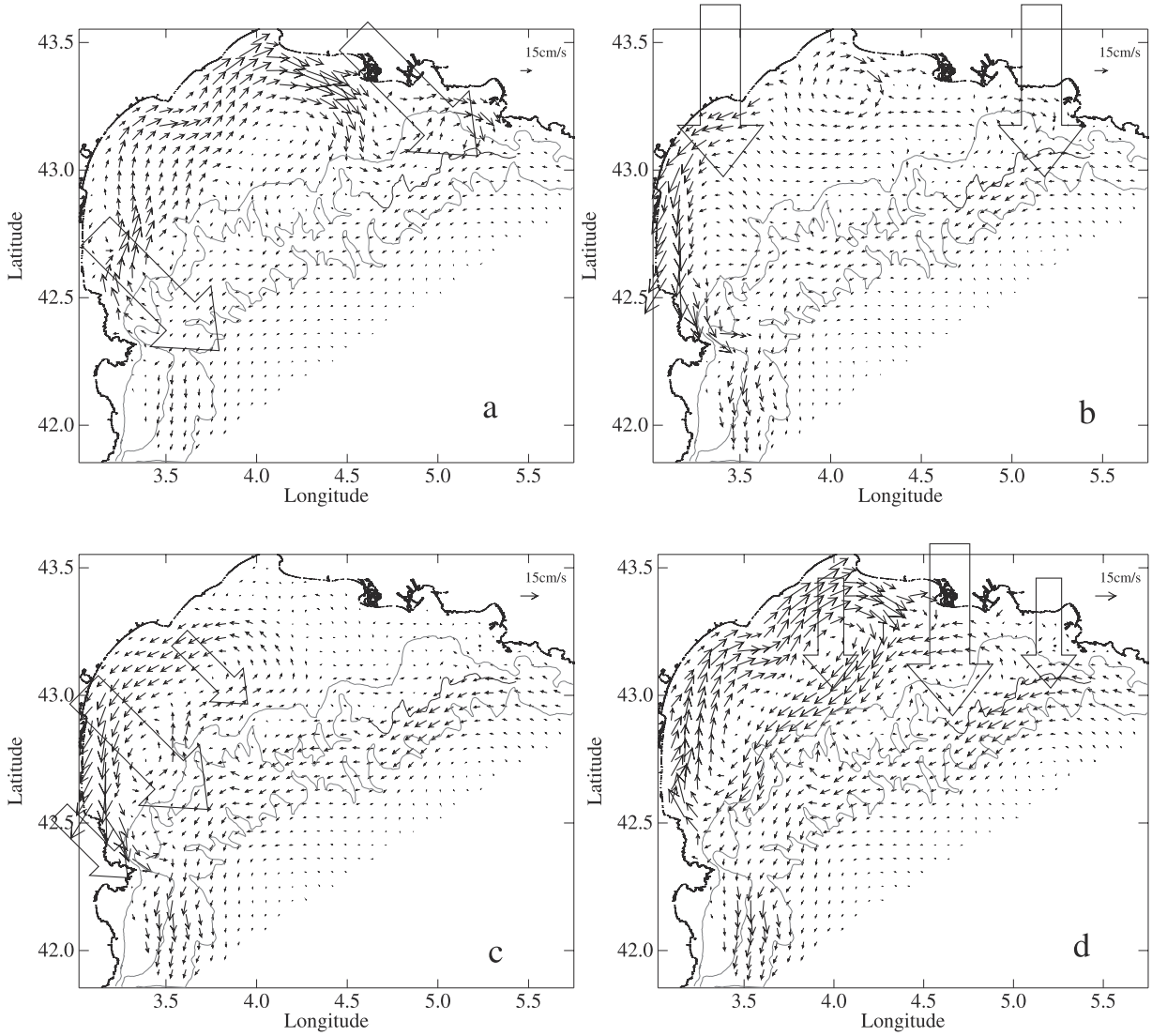

Figure 12. Depth-averaged current fields for different wind direction and structures: (a) homogeneous northwestern wind, (b) homogeneous northern wind, (c) inhomogeneous northwestern wind (Tramontane), (d) inhomogeneous northern wind (Mistral). The large arrows represent the wind field.

related to the position of the shelf break which constrains the offshore extension of the wind-induced eddies. A simulation with a flat bottom on the whole model domain shows that the anticyclonic eddy as well as the small cyclonic eddy located at the south of the Rhone extend offshore up to the southern open boundary (the simulation is not presented here because of the sensitivity of the result to the position of the open boundary).

[48] On the basis of the academic simulations of Figure 12, the observed and modeled circulation during the first survey (Figures 9a and 11a) can be reasonably interpreted as the result of the juxtaposition of the effect of the Mistral and Tramontane curls (Figures 12c and 12d). During the second period, the weakening of the Tramontane produces a wind field with a predominant Mistral component (Figure 11d). The observed and modeled circulations for this latter period (Figures 9b and 11c) agree reasonably well with the academic simulation with Mistral only (Figure 12d).

[49] This study emphasizes the critical need of an accurate knowledge of the spatial structure of the wind to model the oceanic circulation on the shelf, since the wind curl rather than the wind direction forces the direction of the coastal currents.

4.2. Exchanges of Water on the Shelf

[50] The in-situ observations show the presence of various water masses on the shelf:

1. though the Rhône river discharges during March 1998 are relatively low and the strong winds favor the dilution of the freshwater plume, the region of freshwater influence extends over a large area and is still visible at 100 km southwest of the river mouth.
2. cold and less saline water takes place near the bottom south of the Camargue,
3. tongues of relatively warm and salty slope waters penetrate onto the shelf. Although the characteristics of these waters are mostly marked near the bottom, the SST

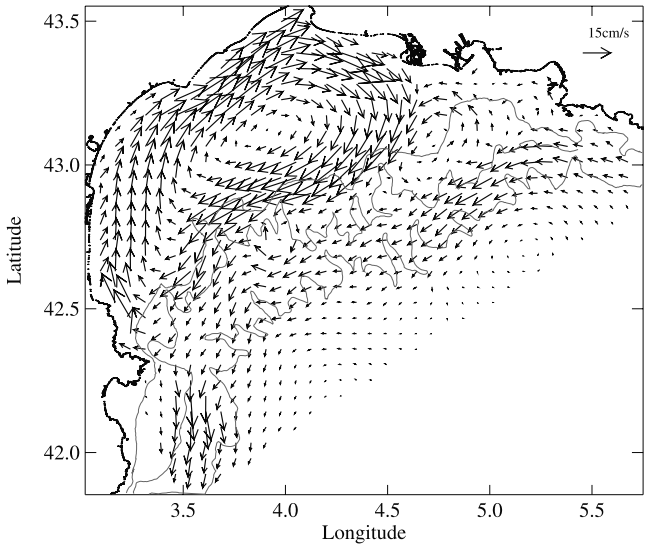

Figure 13. Depth-averaged current field for an inhomogeneous northern wind (Mistral) and a 100m deep flat bottom on the continental shelf.

also identifies them on the eastern and western part of the shelf.

As the simulation reproduces these various bodies of water, we use the model output to find the mechanisms responsible of their formation and spreading.

4.2.1. Intrusion of Slope Water Onto the Shelf

[51] In so far as the Coriolis parameter can be considered constant, coastal currents tend to follow the isobaths because of vorticity conservation constraints [*Mertz and Wright*, 1992]. On continental shelves, constant wind also tends to produce along-coast currents, which, in the case of an ideally rectilinear coastline, have no cross-shelf net transport [*Csanady*, 1982]. In the previous section, it has been seen that inhomogeneous wind field and irregular bathymetry induce complex circulations. For instance, in the case of northern wind (Figure 12b), the southward coastal current exports water out of the Gulf of Lion. Compensations by offshore waters intrusions are achieved through cross-slope currents driven by the eddy circulation on the shelf. For a uniform northwestern wind (Figure 12a), slope water originating from the Liguro-Provençal Current penetrates onto the southwestern shelf and exits it mostly in its northeastern part, thus going back to the slope. The two last academic simulations (Figures 12c and 12d) with nonuniform winds have a different impact on the shelf-slope exchanges, with a strong export of shelf water for the Tramontane situation and very little cross-slope exchange for the Mistral situation.

[52] The two realistic simulations of 16 and 20 March (Figure 11), that embrace the two latter cases, reveal the shelf-slope exchanges that take place during the two surveys. On 16 March, the combined effect of the Mistral and the Tramontane induces a cyclonic circulation in the west and an anticyclonic circulation in the north. Following the outflow of coastal water at the southwestern limit of the shelf, compensating flows of slope water penetrate onto the shelf south of the Rhône delta and also at the latitude of Sète, where it is advected toward the coast by eddy circulations. On 20 March, the predominance of the Mistral significantly changes the shelf circulation and reduces the shelf-slope exchanges because the large anticyclonic cell that develops over most of the shelf tends to isolate the coastal water from the slope waters.

4.2.2. Genesis and Spreading of Cold Water

[53] Winter formation and cascading of dense cold water is a well-known mechanism in the Gulf of Lion because of cooling and evaporation caused by the continental cold and dry winds [*Lacombe and Tchernia*, 1974]. During the FETCH experiment, the coldest waters are localized south of the Rhône delta where the heat loss is maximum. In this area, on the 14–15 March, the thermosalinograph measures minimum surface temperature and salinity (θ = 12.5°C and S = 37.7), close to the characteristics of the cold water found near the bottom on the mid and outer shelf (θ = 12.6°C and S = 37.8). Spreading of this cold dense water is linked to buoyancy effect and also to the wind-driven circulation. Indeed, a simulation with only the wind-forcing (no heat surface flux and freshwater supply) yields a spreading of the coastal water to the southwest, as well as an upwelling of slope water near the bottom, similar to the realistic simulation. Two concurrent transport processes—both related to the anticyclonic shelf circulation—seem to control the presence of cold water near the bottom.

[54] First, due to an eastward shift of the meteorological fields on 14 March, the anticyclonic eddy moves to the east. The cross shelf branch of the latter leads to offshore advection and downwelling of cold coastal waters. Second, downwelling processes occur in the convergence area between the southward eddy circulation and the southwestward wind driven surface current in the region of the Rhône delta. This could explain the deepening of the fresh surface layer observed at stations 38 and 39 (Figure 7b).

[55] The simulation allows us to examine the fate of the bottom cold water. According to the computed circulation (Figure 11b), after they have reached the external shelf, the cold waters should be entrained to the southwest by eddy circulation according to the current measurement at 60m near station 37 (Figure 10a). Thus, most of cold waters are trapped on the continental shelf especially since their offshore progression would be limited by opposing upwelling currents on the slope evidenced by northwestward current observed south of station 36 (Figure 10a).

5. Conclusions

[56] A first conclusion is that the 3-D oceanic simulation of the FETCH experiment reproduces the main characteristics noticed in the different observations (hydrology and currents). The accuracy and the high resolution (in space and time) of the atmospheric fluxes (especially the wind stress) is primarily responsible of the good results of the simulation on the continental shelf. The databased initialization of the large scale circulation and density field allowed also to represent correctly the shelf—slope exchanges. Quantitative differences have been noted between the observations and the simulation such as the underestimation of the SST by the simulation along the western coast of the Gulf. Reasons probably lie in the uncertainties in initial conditions and also in atmospheric fluxes: the model starts 8 days before the first measurements with an homogeneous temperature field on the shelf which does not allow to estimate the uncertainties

during the spin-up period. Even during the experiment period, the measurements on board the ship are not fully adapted to check with accuracy the large spatial variations of the atmospheric fluxes (especially near the coast where the largest discrepancies between the simulated and observed SST lie).

[57] It is obvious that if errors stay at an acceptable level for short simulations, they might become unacceptably large for longer (seasonal) simulations. In that latter case, uncertainties in the initial fields are certainly not crucial but at the opposite the consequences of systematic biases in the atmospheric fluxes such as those shown in Figure 3 can be dramatic especially in regions characterized by long residence time of the water masses. An interactive procedure to compute the fluxes, using the sea surface temperature of the hydrodynamic model as in the work of *Castellari et al.* [1998] will likely be efficient to limit the consequences of such biases. Assimilation of satellite SST is probably also an interesting way to deal with these problems provided that meteorological and sea state conditions are not favorable to large skin effects affecting the SST.

[58] Concerning the physical results of this study, the hydrological and current data sets as well as the modeling study using realistic forcing characterize the winter circulation associated with continental winds. The shelf circulation is largely driven by wind. More exactly, the wind curl linked to the continental orography is the key factor that controls the direction of the coastal currents and induces eddy circulation on the shelf. An important consequence is the difficulty to forecast the coastal circulation, even the broadest trends, without a good knowledge of the wind field at mesoscale. In the present case, the wind stress data used to force the oceanic model has a sufficient spatial resolution (0.1°) and temporal resolution (3 h time step) to reproduce the major circulation patterns. The different simulations which have been performed with stationary wind fields show that the circulation can be considered as quasi stationary after two days of forcing. Consequently, it seems that in the case of strong and relatively well established wind field, the coastal circulation is only slightly sensitive to the choice of initial conditions of the simulation. In the absence of a similar study for stratified summer conditions, this conclusion should be limited to winter mixed conditions. This outcome is interesting since it gives some elements of response to the question of predictability of the coastal circulation.

[59] Upwellings of slope water onto the shelf are observed at different locations. These inputs of water compensate the export of shelf water by the wind-driven coastal currents. Again, the knowledge of the wind curl is essential for the quantification of the shelf-slope exchanges. As an example, two different wind regimes occur during the modeled period. Although the average wind speed and direction are relatively comparable, the juxtaposition of the Mistral and Tramontane provokes coastal currents that export shelf water and induce, in turn, compensating inflow of the slope water onto the shelf. The Mistral alone provokes a large anticyclonic circulation extending over most of the shelf, which tends to isolate the shelf water from the slope water.

[60] The dispersion of freshwater from the Rhône river and the strong cooling induced by the Mistral south of the Rhône delta generate a layer of cold and less saline water. The model results indicate that the southwestward spreading of the cold water is associated with the wind-induced anticyclonic eddy. Two processes limit the cascading of this layer of cold water. The freshwater from the Rhône decreases the density of the surface layer and inhibits the cascading. The western part of the shelf is probably more favorable to cascading than the eastern part since it is farther from the freshwater sources. The second process is linked to the upwelling of slope water near the bottom. It is possible that the calm periods following the wind gust favor spreading of the dense water due to the upwelling relaxation.

Appendix A

[61] Concerning the initialization of a free surface coastal model, *Auclair et al.* [2000b] showed that a crude interpolation over the model grid of large scale model outputs, or a fortiori irregularly distributed observations, results in a strong unbalance of the model discrete equations. The beginning of the simulations is then characterized by unrealistic transient processes such as the propagation of gravity waves excited at the coast or over steep topography areas. The solution proposed by *Auclair et al.* [2000b] is to apply an optimal interpolation method based on the linearized model equations. If the full set of equations and variables of the model is used, this inverse method leads to solve an eventually large linear equations system. An interesting compromise between c.p.u. and equilibrium of the initial state can be found if the set of equations and variables is for instance limited to the external mode of the model. In the present paper, the initialization is calculated from a set of linearized equations deduced from the model under the following assumptions:

A1. Rigid Lid Approximation

[62]

$$U = -\frac{\partial \psi}{\partial y}, \quad V = \frac{\partial \psi}{\partial x} \tag{A1}$$

where U and V are the components of the transport and ψ the barotropic stream function.

A2. Parameterization of the Vertical Shear of the Geostrophic Current

[63] Let us consider the following form of the pressure gradient:

$$\Delta p(z) = \Delta p_s + g \int_z^0 \Delta \rho \, dz \tag{A2}$$

where Δp_s is the surface pressure gradient and $\Delta\rho$ the horizontal gradient of density. We followed a method presented by *Cooper and Haines* [1996] in order to simplify (A2). Considering $\rho(z)$ an horizontally homogeneous density field, we may assume that horizontal density gradients result from homogeneous vertical displacements h of the water columns. The pressure gradient may then be approximated by:

$$\Delta p(z) = \Delta p_s + g(\rho(0) - \rho(z))\Delta h \tag{A3}$$

the gradient of vertical displacement Δh may be given using (A3) and a condition of no motion at a prescribed depth *zref*

which may be the depth of the bottom as in the work of *Cooper and Haines* [1996]:

$$\Delta h = \frac{-\Delta p_s}{g(\rho(0) - \rho(zref))} \tag{A4}$$

Finally we obtain the relationship:

$$\Delta p(z) = R(z)\Delta p_s = R(z) g \rho_0 \Delta \eta \tag{A5}$$

with

$$R(z) = \frac{\rho(z) - \rho(zref)}{\rho(0) - \rho(zref)} \tag{A6}$$

$R(z)$ was first determined using (A6) and the CTD density sections. We can see from (A5) that $R(z)$ can be considered as a nondimensional form of the vertical shear of the geostrophic current. The validity of our basic assumption (Δh is vertically uniform) was then examined thanks to a comparison of $R(z)$ with geostrophic calculations performed from hydrographic data. Finally, we concluded that $R(z)$ was better estimated by:

$$R(z) = \frac{V_g(z)}{V_g(0)} \tag{A7}$$

where V_g is the mean geostrophic current modulus. Geostrophic currents were calculated from CTD data located in the region of the Liguro-Provençal current, using a classical level of no motion at the bottom [*Durrieu de Madron et al.*, 1992].

A3. Equilibrated Linearized Transport Equations

[64] Neglecting advective terms and taking (A5) into account, the equilibrated equations of the external mode are given by:

$$-f\frac{\partial \psi}{\partial x} = -g\bar{R}\frac{\partial \eta}{\partial x} + \frac{\tau_{sx} - \tau_{bx}}{\rho_0} - H\left[\frac{\partial}{\partial x}K_h\frac{\partial}{\partial x}\left(\frac{1}{H}\frac{\partial \psi}{\partial y}\right) + \frac{\partial}{\partial y}K_h\frac{\partial}{\partial y}\left(\frac{1}{H}\frac{\partial \psi}{\partial y}\right)\right] \tag{A8}$$

$$-f\frac{\partial \psi}{\partial y} = -g\bar{R}\frac{\partial \eta}{\partial y} + \frac{\tau_{sy} - \tau_{by}}{\rho_0} + H\left[\frac{\partial}{\partial x}K_h\frac{\partial}{\partial x}\left(\frac{1}{H}\frac{\partial \psi}{\partial x}\right) + \frac{\partial}{\partial y}K_h\frac{\partial}{\partial y}\left(\frac{1}{H}\frac{\partial \psi}{\partial x}\right)\right] \tag{A9}$$

where τ_s is the wind stress, τ_b the bottom stress, H is the bottom depth, K_h is the horizontal viscosity coefficient (cf. section 2.2.1) and $\bar{R} = \int_{-H}^{0} R\, dz$.

The bottom stress, usually parameterized by a quadratic law of the bottom current, is here given by a linear relation (τ_{bx}, τ_{by}) = $\rho_0 c_d(u_b, v_b)$, the bottom current is estimated from the transport and the vertical shear of the geostrophic current using the relationship:

$$(u_b, v_b) = \frac{R_{(z=-H)}}{\bar{R}}(U, V) = \frac{R_{(z=-H)}}{\bar{R}}\left(-\frac{\partial \psi}{\partial y}, \frac{\partial \psi}{\partial x}\right) \tag{A10}$$

If (A8) and (A9) are divided by $\bar{R}$, then derived with respect to y and x respectively and then (A8) subtracted from (A9), the surface elevation can be eliminated. Using (A10), an equation for the stream function ψ can be finally obtained. Practically a linear equation system of the following type:

$$A\Psi = B \tag{A11}$$

is numerically solved on the model grid. Ψ is a column matrix containing the stream function values at each grid point. The square matrix A contains the operators of the stream function that are deduced from the linearized schemes of the external mode of the model. The column matrix B contains the forcing terms namely the curl of $\frac{\tau_s}{\rho_0 \bar{R}}$ and the boundary conditions.

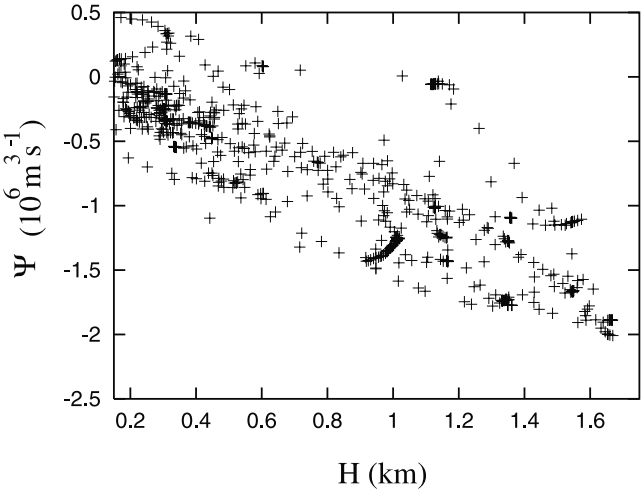

Figure A1. Stream function estimated from the ADCP currents as a function of topography.

A4. Boundary Conditions

[65] The stream function vanishes at the coast. The problem of the open boundary was rather tricky insofar as we did not have outputs of a large scale model to specify the boundary values of the stream function. General characteristics of the northwestern Mediterranean which have been reported by numerous authors over the last 20 years (see, for instance, *Millot* [1990]) were nevertheless introduced at the open boundaries in a simplified manner. The assumption that the Liguro-Provençal current mainly followed the continental slope led us to prescribe a bottom depth dependent relationship. Practically the boundary stream function has been set to:

$$\psi_{ob} = \alpha H \tag{A12}$$

The choice of a linear function is very simple but seems justified if we consider the stream function estimated from the ADCP currents (Figure A1). The stream function was calculated along the cross-shelf transects from an estimation of the transport based on the vertical profile of the alongshelf component of the current. The current profile was extrapolated under the deepest ADCP measurements using the function $R(z)$. Obviously the accuracy of this calculation is questionable insofar as the ADCP current can

not be considered as non divergent. The result is sensitive to the filtering of the high frequencies of the ADCP currents and also to the way of extrapolating the current in order to estimate the transport. However, in all cases the assumption of linearity seemed acceptable. The intensity of the slope current calculated from (A11) is highly dependent on the value of α (on the opposite the shelf circulation is rather dependent on the wind stress). Practically α was empirically set to 400 s^{-1} in order to reproduce the magnitude of the observed currents and density gradients in the region of the Liguro-Provençal current.

[66] As the simplicity of (A12) may induce some unrealistic adjustment of the solution in the vicinity of the boundary, it has been decided to solve (A11) on an extended domain.

A5. Initialization of the Model

[67] Let ψ_{t0} be a solution of (A11). The components of the transport, (Ut_0, V_{t0}) are deduced from ψ_{t0} using (A1). The components of the current are deduced from the transport and the vertical shear parameterization R:

$$(u_{t0}, v_{t0}) = \frac{R_{(z)}}{\overline{R}}(U_{t0}, V_{t0}) \tag{A13}$$

Transport and current values are then introduced in (A8) and (A9) in order to calculate the surface elevation. Similarly to (A11), (A8), and (A9) are used to form an overdetermined system of linear equations solved on the model grid:

$$CX = D \tag{A14}$$

where X is a column matrix containing the surface elevation value at each grid point. The matrix C contains the horizontal gradient operators of the surface elevation, and D the remaining terms of (A8) and (A9), i.e., the Coriolis term, the bottom and wind stresses and the horizontal viscosity. Solution of (A14) is

$$X = \left(C^T C\right)^{-1} C^T D \tag{A15}$$

A perturbation of the density field can be deduced from the surface elevation, using the hydrostatic equilibrium assumption and (A5) derived with respect to z:

$$\rho_{t0} = -\rho_0 R' \eta_{t0} \tag{A16}$$

where R' is the derivative of R with respect to z. The total density field is given by

$$\rho = \rho(z) + \rho_{t0} \tag{A17}$$

where the horizontally homogeneous density field, $\rho(z)$, is chosen to be representative of the simulated case, namely determined from the FETCH CTD data. The initial salinity field, S_{t0} is given by a function of density empirically determined from the set of CTD data. The temperature field, T_{t0}, is finally computed using the model equation of state.

[68] The complete field is then used as an initial state for the simulations. In agreement with conclusions of *Auclair et al.* [2000b], the initial state is stable and does not produce significant transient adjustment processes at the beginning of the simulation.

[69] **Acknowledgments.** We acknowledge the financial support from EC-MAST Program through the METRO-MED contract (MAS3-CTP96-0049), and from the CNRS-INSU through the PNEC and PATOM programs. Linear systems described in the annex were solved using SCILAB software. We warmly thank the officers and crews of R/V *L'Atalante* from Ifremer for their assistance. We thank J. L. Devenon, A. Lapouyade and D. Taillez for their hard work at sea. Daniele Hauser and all the participants to the FETCH experiment are acknowledged.

References

Auclair, F., P. Marsaleix, and C. Estournel, Sigma coordinate pressure gradient errors: Evaluation and reduction by an inverse method, *J. Atmos. Oceanic Technol.*, *17*, 1348–1367, 2000a.

Auclair, F., S. Casitas, and P. Marsaleix, Application of an inverse method to coastal modeling, *J. Atmos. Oceanic Technol.*, *17*, 1368–1391, 2000b.

Beckers, J. M., *La Méditerranée occidentale: De la modélisation mathématique à la simulation numérique*, Collect. des publ. de la Fac. des Sci. Appl. no. 136, 342 pp., Univ. of Liège, Liège, Belgium, 1995.

Blumberg, A. F., and G. Mellor, A description of a three dimensional coastal circulation model, in *Three Dimensional Coastal Ocean Model*, edited by N. Heaps, 208 pp., 1987.

Castellari, S., N. Pinardi, and K. Leaman, A model study of air-sea interactions in the Mediterranean Sea, *J. Mar. Syst.*, *18*, 89–114, 1998.

Cooper, M., and K. Haines, Altimetric assimilation with water property conservation, *J. Geophys. Res.*, *101*, 1059–1077, 1996.

Csanady, G. T., *Circulation in the Coastal Ocean*, D. Reidel, Norwell, Mass., 1982.

Durrieu de Madron, X., A compilation of ship-borne and moored ADCP data from the FETCH experiment—March 13–April 15, 1998, *Doc. FETCH No. 09*, 27 pp., 1999.

Durrieu de Madron, X., F. Nyffeler, E. T. Balopoulos, and G. Chronis, Circulation and distribution of suspended matter in the Sporades Basin (northwestern Aegean Sea), *J. Mar. Syst.*, *3*, 237–248, 1992.

Estournel, C., V. Kondrachoff, P. Marsaleix, and R. Vehil, The plume of the Rhone: Numerical simulation and remote sensing, *Cont. Shelf Res.*, *17*, 889–924, 1997.

Estournel, C., P. Broche, P. Marsaleix, J. L. Devenon, F. Auclair, and R. Vehil, The Rhone river plume in unsteady conditions: Numerical and experimental results, *Estuarine Coastal Shelf Sci.*, *53*, 25–38, 2001.

Flexas, M., M. A. Garcia, X. Durrieu de Madron, M. Canals, and P. Arnau, Flow variability in the Gulf of Lions during the MATER HFF Experiment (March–May 1997), *J. Mar. Syst.*, *33–34*, 197–214, 2002.

Gaspar, P., Y. Gregoris, and J. M. Lefevre, A simple eddy kinetic energy model for simulations of the oceanic vertical mixing: Tests at station Papa and long-term upper ocean study site, *J. Geophys. Res.*, *95*, 179–193, 1990.

Hall, J., and S. Smith, First report of the JGOFS/LOICZ continental margins task team. LOICZ reports and studies no 7, *JGOFS Rep. No. 21*, 1996.

Hauser, D., et al., The FETCH experiment: An overview, *J. Geophys. Res.*, *108*, doi:10.1029/2001JC001202, in press, 2003.

Herbaut, C., F. Martel, and M. Crépon, A sensitivity study of the general circulation of the western Mediterranean sea, 2, The response to atmospheric forcing, *J. Phys. Oceanogr.*, *27*, 2126–2145, 1997.

Hua, B. L., and F. Thomasset, A numerical study of the effects of coastline geometry on wind-induced upwelling in the Gulf of Lions, *J. Phys. Oceanogr.*, *13*, 678–694, 1983.

Joyce, T. M., On in situ "calibration" of shipboard ADCPs, *J. Atmos. Oceanic Technol.*, *6*, 169–172, 1989.

Lacombe, H., and P. Tchernia, Les zones de formation d'eau profonde océanique: Caractères—processus—problèmes, in Processus de formation des eaux océaniques profondes, *Colloq. Int. Centre Natl. Rech. Sci.*, *215*, 249–262, 1974.

Madec, G., F. Lott, P. Delecluse, and M. Crépon, Large-scale preconditioning of deep-water formation in the northwestern Mediterranean sea, *J. Phys. Oceanogr.*, *26*, 1393–1408, 1996.

Marsaleix, P., C. Estournel, V. Kondrachoff, and R. Vehil, A numerical study of the formation of the Rhone river plume, *J. Mar. Syst.*, *14*, 99–115, 1998.

Mertz, G., and D. G. Wright, Interpretations of the JEBAR term, *J. Phys. Oceanogr.*, *22*, 301–305, 1992.

Millero, F. J., and A. Poisson, International one-atmosphere equation of state of seawater, *Deep Sea Res.*, *28*, 625–629, 1981.

Millot, C., The Gulf of Lions' hydrodynamics, *Cont. Shelf Res.*, *10*, 885–894, 1990.

Oey, L. Y., and P. Chen, A model simulation of circulation in the northeast Atlantic shelves and seas, *J. Geophys. Res.*, *97*, 20,087–20,115, 1992.

Pollard, R., and J. Read, A method for calibrating shipmounted Acoustic Doppler Profilers and the limitations of Gyro Compasses, *J. Atmos. Oceanic Technol.*, *6*, 859–865, 1989.

Taillez, D., J. L. Devenon, X. Durrieu de Madron, and A. Lapouyade, Données hydrologiques de l'Atalante, *Doc. FETCH No. 08*, 156 pp., 1999.

F. Auclair, C. Estournel, C. Julliand, P. Marsaleix, and R. Vehil, Laboratoire d'Aérologie, Centre National de la Recherche Scientifique-Université Paul Sabatier, UMR 5560, 14 Avenue Edouard Belin, 31400 Toulouse, France. (claude.estournel@aero.obs-mip.fr)

X. Durrieu de Madron, CEFREM, Centre National de la Recherche Scientifique-Université de Perpignan, UMR 5110, 52 Avenue de Villeneuve, 66860 Perpignan, France.

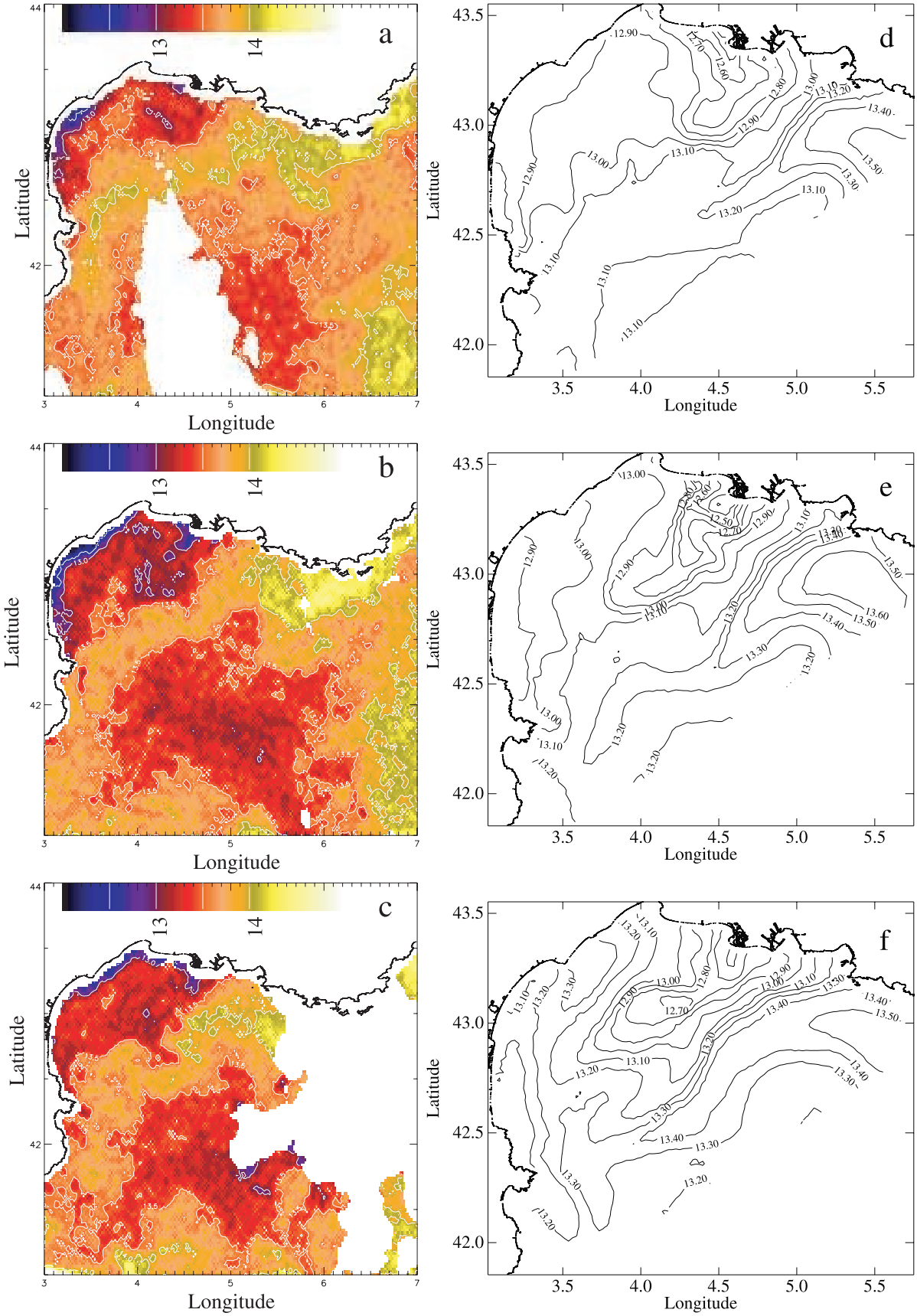

Figure 5. Comparison of the observed and simulated sea surface temperatures. AVHRR SST images for the 14 March 1998 (a), 17 March 1998 (b) and 21 March 1998 (c). Simulated SST distribution for the 14 March 1998 (d), 17 March 1998 (e) and 21 March 1998 (f).